

BEV-ODOM2: Enhanced BEV-based Monocular Visual Odometry with PV-BEV Fusion and Dense Flow Supervision for Ground Robots

Yufei Wei¹, Wangtao Lu¹, Sha Lu¹, Chenxiao Hu¹, Fuzhang Han², Rong Xiong¹ and Yue Wang^{1†}

Abstract—Bird’s-Eye-View (BEV) representation offers a metric-scaled planar workspace, facilitating the simplification of 6-DoF ego-motion to a more robust 3-DoF model for monocular visual odometry (MVO) in intelligent transportation systems. However, existing BEV methods suffer from sparse supervision signals and information loss during perspective-to-BEV projection. We present BEV-ODOM2, an enhanced framework addressing both limitations without additional annotations. Our approach introduces: (1) dense BEV optical flow supervision constructed from 3-DoF pose ground truth for pixel-level guidance; (2) PV-BEV fusion that computes correlation volumes before projection to preserve 6-DoF motion cues while maintaining scale consistency. The framework employs three supervision levels derived solely from pose data: dense BEV flow, 5-DoF for the PV branch, and final 3-DoF output. Enhanced rotation sampling further balances diverse motion patterns in training. Extensive evaluation on KITTI, NCLT, Oxford, and our newly collected ZJH-VO multi-scale dataset demonstrates state-of-the-art performance, achieving 40% improvement in RTE compared to previous BEV methods. The ZJH-VO dataset, covering diverse ground vehicle scenarios from underground parking to outdoor plazas, is publicly available to facilitate future research.

Index Terms—Monocular visual odometry, bird’s-eye-view representation, dense optical flow supervision, ground vehicle navigation, scale drift reduction

I. INTRODUCTION

BIRD’S-EYE-VIEW (BEV) representation has become a cornerstone for perception and localization tasks in modern intelligent transportation systems [1]–[3], offering a powerful solution to the scale drift problem inherent in Monocular Visual Odometry (MVO) [4], [5]. For ground vehicles like autonomous cars and logistics robots, motion is predominantly planar [6]. This allows for simplifying pose estimation from six degrees of freedom (6-DoF) to a more robust 3-DoF model (x, y, yaw), which naturally aligns with the unified, metric-scaled grid of BEV representation [7]. This simplification not only reduces computational complexity but also mitigates the accumulation of errors in non-primary motion axes, a common source of drift in long-range navigation.

BEV-ODOM [8] demonstrates that a BEV-based framework can effectively reduce scale drift using only 3-DoF pose supervision, eliminating the need for auxiliary tasks like depth estimation [9] or semantic segmentation [10], which add complexity and data collection costs. However, this and other BEV-based approaches face two critical limitations. First, the supervision signal from a single 3-DoF pose vector is sparse, providing insufficient guidance for the network to learn fine-grained, pixel-level correspondences between consecutive BEV feature maps. As recent works like DUStr3R [11] have shown, dense supervision is crucial for achieving a robust geometric understanding of motion. Second, the standard

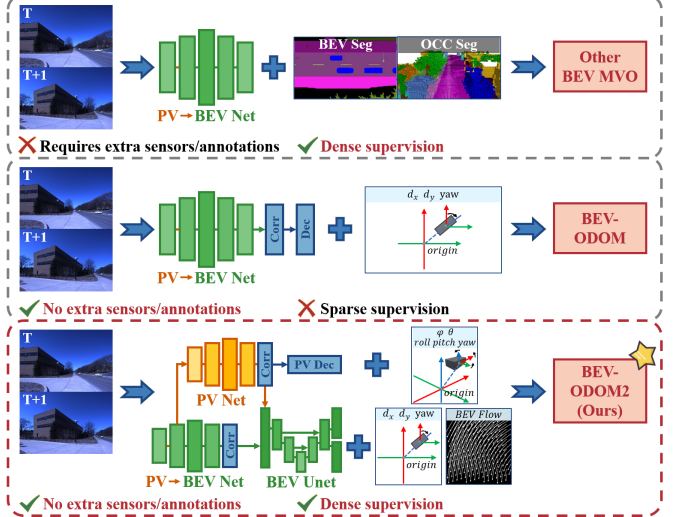


Fig. 1: Comparison of BEV-based monocular odometry methods. Unlike prior approaches needing extra annotations or limited by sparse supervision, our BEV-ODOM2 leverages PV-BEV fusion and dense BEV flow to provide rich supervision from pose data alone.

transformation from perspective view (PV) to BEV, often implemented with architectures like Lift-Splat-Shoot (LSS) [12], [13], inherently causes information loss. By projecting 3D information onto a 2D plane, these methods discard geometric cues related to non-primary degrees of freedom (pitch, roll, and z-axis translation). This loss can create ambiguity in odometry estimation; for instance, road irregularities or vehicle dynamics can cause changes in pitch or roll that are invisible in the BEV representation, which can cause the network to learn inconsistent motion patterns, thereby degrading performance.

To overcome these challenges, we propose a dual-strategy approach that enhances BEV-based odometry without introducing new types of external supervision. To address the sparse supervision problem, we introduce dense BEV optical flow supervision. A key insight is that due to the unified metric scale of the BEV grid, the dense optical flow between two frames can be constructed directly from the ground truth 3-DoF relative pose transformation. This provides a dense, pixel-level training signal that guides the network to learn detailed feature correspondences, using only the existing pose data.

To compensate for the information loss, we introduce a PV-BEV dual-branch fusion strategy. We add a parallel branch that computes a correlation-based cost volume from PV features [14], [15] before the LSS projection occurs. This PV cost volume effectively captures the rich 6-DoF motion signatures

at a feature level. It is then projected into the BEV space using the same LSS pipeline and fused with the BEV-native correlation features. This architecture allows our model to leverage the geometric richness of the perspective view while retaining the scale consistency and efficiency of the 3-DoF BEV representation.

Based on these insights, we present BEV-ODOM2, an enhanced monocular visual odometry framework that integrates this dual-strategy approach into a unified, end-to-end architecture. Our method preserves the robust scale consistency and suppression of cumulative drift inherent to BEV-based odometry, while achieving superior accuracy by incorporating dense supervision and preserving 6-DoF motion information. Critically, all supervision signals are constructed from the pose ground truth alone. This multi-level supervision scheme includes dense BEV optical flow for correspondence learning, a 5-DoF pose for the PV branch, and a 3-DoF pose for the final output. The 5-DoF supervision consists of the full rotation and a scale-free translation direction, which maintains geometric consistency within the monocular framework. Furthermore, the framework incorporates targeted data augmentation strategies to enhance robustness across the diverse motion patterns encountered in real-world transportation scenarios.

In addition, we introduce the ZJH-VO dataset, a new ground-vehicle odometry dataset that covers multiple scenes and scales, addressing the lack of publicly available benchmarks with such diversity. We use ZJH-VO to evaluate the generalization ability of BEV-ODOM2, and we have released the dataset to the community to support future research.

Our contributions can be summarized as follows:

- We propose BEV-ODOM2, a novel MVO framework that uses a unified dual-strategy approach to address the core limitations of sparse supervision and information loss in existing BEV-based methods, achieving state-of-the-art, scale-consistent performance without requiring auxiliary supervision.
- We introduce two key technical innovations: a dense BEV optical flow supervision module that leverages the constructible nature of BEV from pose transformations, and a PV-BEV dual-branch fusion strategy that preserves essential 6-DoF motion information by projecting feature-level correlation volumes.
- We develop specialized data augmentation techniques that target dataset biases common in transportation scenarios, including enhanced sampling of large rotations and extended temporal sampling to improve robustness to diverse vehicle dynamics.
- We construct the ZJH-VO dataset, a multi-scene and multi-scale benchmark for ground-vehicle odometry, which fills the gap of existing datasets lacking such diversity. We validate BEV-ODOM2 on ZJH-VO in addition to NCLT [16], Oxford [17], and KITTI [18], demonstrating robust performance across diverse motion scenarios. The ZJH-VO dataset is publicly available to the community at <https://github.com/WeiYuFei0217/ZJH-VO-Dataset/>.

II. RELATED WORK

This section reviews existing literature on visual odometry, categorized into traditional geometric methods, learning-based methods in the perspective view, and emerging learning-based methods that leverage the BEV representation.

A. Traditional Methods

Traditional MVO methods are founded on geometric principles and are highly interpretable. These approaches are typically classified as feature-based, direct, or semi-direct. Feature-based methods, such as ORB-SLAM3 [19], detect and match sparse keypoints across consecutive frames to estimate egomotion. Direct methods, like DSO [20], minimize photometric errors over a set of pixels, offering high precision in textured environments. Semi-direct methods, exemplified by SVO [21], combine the efficiency of direct tracking with the robustness of feature-based optimization.

A fundamental challenge for all traditional MVO systems is scale ambiguity. These methods establish scale through initial depth estimates from the first few frames, using them as global references. However, calibration errors, feature mismatches, and motion blur lead to error accumulation during iterative pose updates, resulting in severe scale drift that limits their effectiveness in long-distance navigation tasks.

B. Learning-Based Methods Under Perspective View

Learning-based PV methods have emerged as a powerful alternative, leveraging deep neural networks to overcome the limitations of traditional approaches, particularly in scale estimation. Early works, such as DeepVO [22], demonstrate the feasibility of using end-to-end recurrent convolutional neural networks to directly regress pose from image sequences. However, these methods often lacked geometric interpretability, limiting their generalization capabilities.

Subsequent research focuses on integrating geometric constraints with deep learning to improve upon early end-to-end regression models. One prominent approach involves incorporating auxiliary supervision through side-tasks. For instance, methods like TartanVO [23] and DF-VO [24] utilize depth and optical flow supervision to provide the network with explicit geometric cues for scale anchoring and accuracy enhancement. A further development in this area involves tightly coupling learned feature representations with geometric optimization within a single architecture. Systems such as DROID-SLAM [25] and its successor DPVO [26] implement this by combining dense correlation volumes with a differentiable bundle adjustment layer, enabling the joint optimization of pose and structure.

Despite their significant advancements, a common limitation of these perspective-view methods is their reliance on auxiliary supervision, such as from depth, optical flow, or stereo data, to ensure scale consistency. This reliance increases the cost and complexity of data collection and annotation.

C. Learning-Based Methods Under BEV Representation

Leveraging the common ground-plane assumption for ground vehicles, BEV representation has emerged as a promising paradigm for MVO [12]. The inherent properties of BEV's unified metric-scaled grid enable a natural reduction from 6-

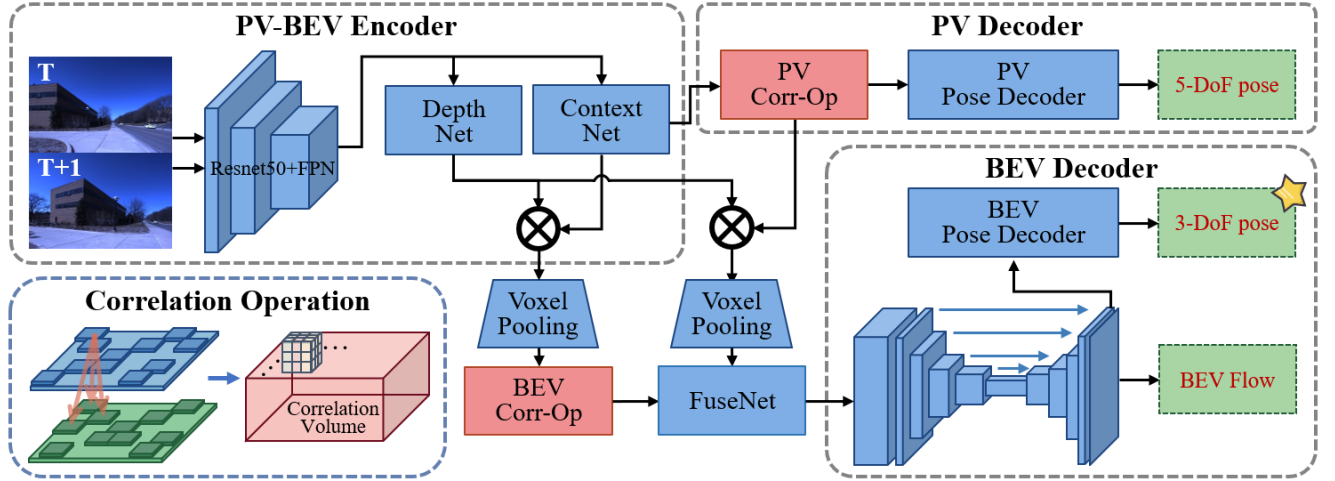


Fig. 2: Overview of the proposed framework.

DoF to 3-DoF pose estimation, establishing an implicit scale anchoring mechanism through the consistent spatial resolution of the grid structure.

Initial BEV-based odometry approaches primarily focus on semantic-level understanding for motion estimation. BEV-SLAM [1] constructs semantic BEV representations through CNNs and performs localization by matching against pre-existing semantic maps. BEV-Locator [3] transforms perspective imagery into BEV encodings and employs cross-modal transformers for semantic feature alignment. OCC-VO [27] extends this paradigm to volumetric space, generating 3D semantic occupancy representations from multi-view inputs for global map registration.

While this approach demonstrates the potential of BEV, its performance is fundamentally tied to the accuracy of the intermediate map generation, which requires costly and extensive annotation for supervision.

Recognizing these limitations, recent advances explore direct motion estimation in BEV space without semantic dependencies. BEV-ODOM [8] demonstrates that a BEV-based framework using correlation-based regression can effectively learn to estimate ego-motion with strong scale consistency without any auxiliary supervision. Subsequently, BEV-DWPVO [7] improves upon this by replacing the regression backend with a more interpretable pipeline, which extracts and matches keypoints in the BEV space and computes the final pose using a differentiable weighted Procrustes solver [28].

While these pose-only methods achieve notable scale consistency, they directly optimize with sparse pose supervision without leveraging the constructible nature of BEV representation for richer guidance. Additionally, the standard perspective-to-BEV transformation discards non-planar motion information, potentially degrading accuracy in complex driving scenarios. These limitations motivate our proposed BEV-ODOM2, which constructs dense supervision from pose ground truth and employs a dual-branch architecture to preserve perspective-view motion cues while maintaining the scale consistency benefits of BEV representation.

III. METHODOLOGY

Ground vehicles in intelligent transportation systems primarily operate under constrained planar motion, enabling the simplification of pose estimation from 6-DoF to 3-DoF while focusing on the essential motion components for autonomous navigation [6], [8]. Building upon this principle, we present BEV-ODOM2, an enhanced BEV-based monocular visual odometry framework that addresses two critical limitations in existing approaches: sparse supervision signals that inadequately guide correlation learning [5], and information loss during perspective-to-BEV transformation. Our solution employs a dual-strategy approach combining dense BEV optical flow supervision with PV-BEV dual-branch fusion, where all supervision signals are constructed directly from pose ground truth without requiring additional sensor modalities.

A. Overall Framework

Fig. 2 illustrates the overall architecture of BEV-ODOM2. The system processes consecutive monocular images I_t and I_{t+1} through parallel processing branches that extract complementary motion information. The perspective view (PV) branch captures rich 6-DoF motion patterns through correlation operations before LSS transformation [12], while the BEV branch performs correlation operations on unified metric-scaled features for final 3-DoF pose estimation. The core innovation lies in projecting PV-derived correlation cost volumes into BEV space through the LSS pipeline, and then concatenating them with BEV correlation cost volumes to fuse relative motion features from both representations.

The framework employs three supervision strategies, all derived from pose ground truth: (1) dense BEV optical flow supervision that exploits the constructible property of BEV representation for pixel-level motion learning, (2) 5-DoF pose supervision for the PV branch (excluding scale to maintain consistency with monocular constraints), and (3) 3-DoF pose supervision for the final output. This multi-level supervision scheme ensures comprehensive motion information extraction while avoiding the need for additional supervisory modalities beyond pose ground truth.

B. Feature Extraction and PV Branch

The dual-branch architecture leverages complementary advantages of perspective view and BEV representations to address information preservation challenges inherent in traditional BEV-only approaches. Both branches share a common feature extraction backbone to ensure consistent feature representation while processing motion information through distinct geometric paradigms.

Shared Feature Extraction: The system employs a ResNet-50 [29] backbone integrated with Feature Pyramid Network (FPN) [30] to extract multi-scale hierarchical features $\mathbf{F}_{\text{IF}} \in \mathbb{R}^{C_{\text{IF}} \times H_{\text{PV}} \times W_{\text{PV}}}$ from consecutive input images I_t and I_{t+1} . Camera intrinsic parameters $\mathbf{K} \in \mathbb{R}^{3 \times 3}$ and extrinsic parameters $\mathbf{E} \in \mathbb{R}^{3 \times 4}$ are encoded through a Multi-Layer Perceptron and fused with image features via element-wise multiplication:

$$\mathbf{F}_{\text{PV}} = \mathbf{F}_{\text{IF}} \odot \text{MLP}(\mathbf{K}, \mathbf{E}), \quad (1)$$

where \odot denotes element-wise multiplication and $\mathbf{F}_{\text{PV}} \in \mathbb{R}^{C_{\text{PV}} \times H_{\text{PV}} \times W_{\text{PV}}}$ represents the processed perspective features.

Perspective View Branch Processing: The PV branch extracts correlation-based motion patterns before LSS transformation to preserve essential 6-DoF geometric information that would otherwise be compressed during BEV projection. Following established precedents in optical flow estimation [14], [15], local correlation computation between consecutive perspective features captures pixel-level motion patterns:

$$\mathbf{C}_{\text{PV}}[\Delta x, \Delta y, x, y] = \sum_{c=1}^{C_{\text{PV}}} \mathbf{F}_{\text{PV}}^t[c, x, y] \cdot \mathbf{F}_{\text{PV}}^{t+1}[c, x + \Delta x, y + \Delta y], \quad (2)$$

where $\Delta x, \Delta y \in [-\Delta_{\text{PV}}, \Delta_{\text{PV}}]$ define the local search range, producing correlation volume $\mathbf{C}_{\text{PV}} \in \mathbb{R}^{(2\Delta_{\text{PV}}+1)^2 \times H_{\text{PV}} \times W_{\text{PV}}}$. This correlation volume encodes relative motion patterns at the feature level rather than the spatial level, enabling subsequent projection to BEV space while preserving essential motion signatures.

5-DoF PV Pose Supervision: For comprehensive motion learning, the PV correlation volume undergoes spatial dimension reduction through a sequence of convolutional layers followed by fully connected layers for pose regression:

$$\mathbf{T}_{5\text{-DoF}} = \text{MLP}_{\text{PV}}(\text{CNN}_{\text{PV}}(\mathbf{C}_{\text{PV}})) \quad (3)$$

, where CNN_{PV} represents sequential convolutional downsampling and MLP_{PV} indicates fully connected layers for pose estimation. The output $\mathbf{T}_{5\text{-DoF}} = [\mathbf{R}_5, \mathbf{t}_5]$ represents the 5-DoF transformation with rotation matrix $\mathbf{R}_5 \in \mathbb{R}^{3 \times 3}$ and translation vector $\mathbf{t}_5 \in \mathbb{R}^3$, where scale information is excluded to maintain consistency with monocular visual constraints.

C. BEV Projection Pipeline

The BEV projection process transforms both perspective view features and correlation volumes into a unified metric-scaled representation while preserving essential motion information from different geometric paradigms. This transformation employs the Lift-Splat-Shoot (LSS) architecture [12]

with shared network parameters to ensure consistent geometric mapping across different input modalities.

Perspective Feature to BEV Transformation: The processed perspective features $\mathbf{F}_{\text{PV}} \in \mathbb{R}^{C_{\text{PV}} \times H_{\text{PV}} \times W_{\text{PV}}}$ undergo depth-aware projection to generate BEV representation through a dual-branch refinement process. Two specialized networks further refine the perspective features to predict contextual features and depth distributions, outputting $\mathbf{F}_{\text{PVC}} \in \mathbb{R}^{C_{\text{PV}} \times H_{\text{PV}} \times W_{\text{PV}}}$ and $\mathbf{F}_{\text{PVD}} \in \mathbb{R}^{D_{\text{PV}} \times H_{\text{PV}} \times W_{\text{PV}}}$ respectively, where D_{PV} represents the discretized depth resolution. The contextual and depth features are dimension-expanded to enable element-wise multiplication across channel and depth dimensions:

$$\mathbf{F}_{\text{PVmulti}} = \mathbf{F}'_{\text{PVC}} \odot \mathbf{F}'_{\text{PVD}}, \quad (4)$$

where \mathbf{F}_{PVC} and \mathbf{F}_{PVD} are expanded to $C_{\text{PV}} \times 1 \times H_{\text{PV}} \times W_{\text{PV}}$ and $1 \times D_{\text{PV}} \times H_{\text{PV}} \times W_{\text{PV}}$, and are referred to as \mathbf{F}'_{PVC} and \mathbf{F}'_{PVD} respectively, and \odot denotes element-wise multiplication. This operation produces $\mathbf{F}_{\text{PVmulti}} \in \mathbb{R}^{C_{\text{PV}} \times D_{\text{PV}} \times H_{\text{PV}} \times W_{\text{PV}}}$, which combines contextual features across channels and depth for each pixel. Subsequently, frustum projection maps features at different depths to 3D voxel space, transforms them to the vehicle coordinate system using camera intrinsics and extrinsics, and accumulates them onto the 2D BEV plane. Voxel pooling aggregates these projected features, forming the final BEV feature representation $\mathbf{F}_{\text{BEV}} \in \mathbb{R}^{C_{\text{BEV}} \times H_{\text{BEV}} \times W_{\text{BEV}}}$, where $C_{\text{BEV}} = C_{\text{PV}}$ due to the feature channel preservation during the projection process.

PV Correlation Volume to BEV Projection: A critical innovation lies in projecting the PV correlation volume $\mathbf{C}_{\text{PV}} \in \mathbb{R}^{(2\Delta_{\text{PV}}+1)^2 \times H_{\text{PV}} \times W_{\text{PV}}}$ to BEV space using the identical LSS pipeline and network parameters. This approach is geometrically justified because correlation volumes encode relative motion patterns at the feature level rather than absolute spatial coordinates. The projection process treats each correlation channel as a feature channel, leveraging the same depth distribution \mathbf{F}_{PVD} to map motion patterns to the unified BEV coordinate system:

$$\mathbf{C}_{\text{PV-BEV}} = \text{Project}_{\text{LSS}}(\mathbf{C}_{\text{PV}}, \mathbf{F}_{\text{PVD}}, \mathbf{K}, \mathbf{E}), \quad (5)$$

where \mathbf{K} and \mathbf{E} represent camera intrinsic and extrinsic parameters, respectively. The resulting projected correlation volume $\mathbf{C}_{\text{PV-BEV}} \in \mathbb{R}^{(2\Delta_{\text{PV}}+1)^2 \times H_{\text{BEV}} \times W_{\text{BEV}}}$ preserves 6-DoF motion signatures while conforming to the metric-scaled BEV coordinate system. This shared-parameter projection strategy ensures consistent geometric interpretation across different input modalities while maintaining computational efficiency through parameter reuse.

D. Motion Information Extraction and Fusion

The motion information extraction and fusion process combines correlation-based motion patterns from both BEV and projected PV representations to achieve comprehensive motion understanding while maintaining the computational advantages of 3-DoF pose estimation.

BEV Correlation Computation: Local correlation computation between consecutive BEV features captures planar

motion patterns directly in the unified metric-scaled coordinate system:

$$\mathbf{C}_{\text{BEV}}[\Delta x, \Delta y, x, y] = \sum_{c=1}^{C_{\text{BEV}}} \mathbf{F}_{\text{BEV}}^t[c, x, y] \cdot \mathbf{F}_{\text{BEV}}^{t+1}[c, x + \Delta x, y + \Delta y], \quad (6)$$

where $\Delta x, \Delta y \in [-\Delta_{\text{BEV}}, \Delta_{\text{BEV}}]$ define the local correlation search range, producing $\mathbf{C}_{\text{BEV}} \in \mathbb{R}^{(2\Delta_{\text{BEV}}+1)^2 \times H_{\text{BEV}} \times W_{\text{BEV}}}$. This correlation volume directly encodes planar motion components essential for ground vehicle navigation.

Multi-Modal Correlation Fusion: The projected PV correlation volume $\mathbf{C}_{\text{PV-BEV}}$ and native BEV correlation volume \mathbf{C}_{BEV} are concatenated along the channel dimension to create a comprehensive motion representation:

$$\mathbf{C}_{\text{concat}} = \text{Concat}(\mathbf{C}_{\text{BEV}}, \mathbf{C}_{\text{PV-BEV}}) \in \mathbb{R}^{C_{\text{total}} \times H_{\text{BEV}} \times W_{\text{BEV}}}, \quad (7)$$

where $C_{\text{total}} = (2\Delta_{\text{BEV}}+1)^2 + (2\Delta_{\text{PV}}+1)^2$. This concatenated representation preserves both the scale-consistent planar motion patterns from BEV correlation and the rich 6-DoF motion signatures from projected PV correlation.

Dense Flow Prediction and 3-DoF Pose Estimation: A UNet-style encoder-decoder architecture [31] processes the concatenated correlation features to simultaneously extract and fuse multi-modal motion information while predicting dense flow fields and final pose estimates. The encoder progressively captures global motion patterns from both BEV and projected PV correlations:

$$\mathbf{F}_{\text{Enc}} = \mathbf{U}_{\text{Enc}}(\mathbf{C}_{\text{concat}}). \quad (8)$$

The decoder reconstructs dense BEV optical flow through skip connections that preserve fine-grained correspondence information:

$$\mathbf{F}_{\text{flow}} = \mathbf{U}_{\text{Dec}}(\mathbf{F}_{\text{Enc}}) \in \mathbb{R}^{2 \times H_{\text{BEV}} \times W_{\text{BEV}}}, \quad (9)$$

where \mathbf{F}_{flow} represents the predicted dense BEV optical flow field. Critically, the 3-DoF pose estimation branch connects to the penultimate layer of the flow decoder to leverage the enriched motion features:

$$\mathbf{T}_{\text{3-DoF}} = \text{MLP}_{\text{BEV}}(\text{CNN}_{\text{BEV}}(\mathbf{F}_{\text{Dec}}^{L-1})) = [\theta, t_x, t_y], \quad (10)$$

where $\mathbf{F}_{\text{Dec}}^{L-1}$ denotes the second-to-last decoder layer features, θ represents yaw rotation, and t_x, t_y denote planar translations. This architectural design ensures that dense flow supervision maximally guides the feature learning process for 3-DoF pose regression, as the pose estimation directly utilizes features that have been optimized for pixel-level motion correspondence through flow prediction. The dual-branch fusion within the UNet enables comprehensive utilization of both BEV's scale-consistent planar motion patterns and PV's rich 6-DoF motion signatures, while the dense supervision strategy strengthens the network's capability to capture fine-grained relative motion patterns essential for accurate pose estimation.

E. Dense BEV Optical Flow Supervision

Traditional pose supervision provides sparse signals that may be insufficient for learning fine-grained motion patterns essential for robust visual odometry [5]. We introduce dense BEV optical flow supervision that exploits the geometric consistency and constructible property of BEV representation to

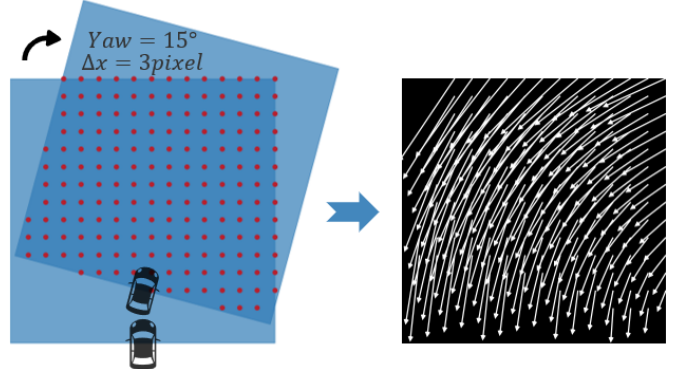


Fig. 3: Construction of the dense BEV optical flow supervision signal from relative pose ground truth.

provide comprehensive pixel-level motion guidance, enabling the network to learn detailed inter-frame correspondences that significantly enhance correlation-based motion estimation.

Unlike perspective view optical flow, which requires complex geometric reasoning across varying depths and viewpoints, BEV optical flow can be directly constructed from pose ground truth due to the unified metric-scaled nature and planar structure of BEV representation, as illustrated in Fig. 3. This constructible property stems from the fact that all BEV features are represented in the ego vehicle coordinate system with consistent metric scaling, enabling direct application of 2D rigid transformations.

Given the relative pose transformation $\mathbf{T}_{\text{rel}} \in \mathbb{R}^{4 \times 4}$ between consecutive frames, which encodes the 3-DoF motion components (yaw rotation and planar translations) in homogeneous coordinates, the ground truth optical flow construction involves a systematic coordinate transformation process. For each BEV pixel at coordinates (u, v) , we first establish the corresponding homogeneous vehicle coordinates:

$$\mathbf{p}_{\text{veh}} = \begin{bmatrix} (o_y - v) \cdot r \\ (u - o_x) \cdot r \\ 0 \\ 1 \end{bmatrix}, \quad (11)$$

where r denotes the BEV resolution (meters per pixel), and (o_x, o_y) represents the pixel coordinates of the vehicle coordinate system origin. The transformed coordinates are obtained through matrix multiplication, and the resulting optical flow is computed as:

$$\mathbf{F}_{\text{flow-gt}}[u, v] = \mathcal{P}(\mathbf{T}_{\text{rel}} \mathbf{p}_{\text{veh}}) - [u, v], \quad (12)$$

where $\mathcal{P}(\cdot)$ denotes the projection operation that converts the transformed homogeneous vehicle coordinates back to pixel coordinates using the inverse mapping of Equation (11).

This construction ensures accurate pixel-level correspondence without requiring external optical flow sensors, additional annotations, or complex depth-dependent geometric computations. The resulting dense flow field $\mathbf{F}_{\text{flow-gt}} \in \mathbb{R}^{2 \times H_{\text{BEV}} \times W_{\text{BEV}}}$ provides comprehensive supervision signals that guide the network to learn fine-grained motion patterns, directly addressing the sparse supervision limitation inherent in pose-only training approaches.

F. Enhanced Rotation Sampling Strategy

To address dataset biases toward straight-line driving scenarios and improve robustness to diverse motion patterns in real-world transportation systems, we implement a targeted sampling strategy that ensures balanced representation of both linear and turning maneuvers while leveraging temporal consistency within driving sequences.

Rotation-Aware Data Augmentation: We construct comprehensive motion pattern databases by preprocessing training sequences to identify frames with diverse rotational characteristics. For each frame in the training dataset, we establish a temporal search window spanning one minute before and after the current timestamp, then extract relative pose transformations for all frame pairs within this window. Frame pairs are categorized based on two criteria: (1) relative yaw angle differences between 15° and 45° are stored in a high-rotation list $\mathcal{L}_{\text{high}}$, while pairs with angular differences below 15° are maintained in a standard-rotation list $\mathcal{L}_{\text{standard}}$, and (2) spatial displacement constraints where only pairs with translation distances up to 4 meters are retained to ensure meaningful correspondence learning.

During training, when a particular frame is selected, the system probabilistically samples from these pre-constructed lists using a 70%-30% distribution, where 70% of samples are drawn from $\mathcal{L}_{\text{high}}$ and 30% from $\mathcal{L}_{\text{standard}}$. This balanced sampling strategy addresses the inherent dataset bias toward straight-line driving by ensuring adequate exposure to challenging rotational motions, while simultaneously preventing over-representation of any single motion pattern that could lead to insufficient training diversity across varied driving scenarios.

Temporal Consistency Benefits: The one-minute temporal window with 4-meter spatial constraints ensures that environmental conditions, lighting characteristics, and scene content remain sufficiently consistent to maintain meaningful correspondence learning, while being large enough to capture reciprocal driving patterns common in transportation infrastructure. For road segments with bidirectional traffic or circular routes, this approach generates training pairs that simulate scenarios with moving objects, environmental changes, and significant rotational variations, effectively augmenting the dataset's diversity without requiring additional data collection efforts.

G. Loss Function Design

The training objective combines multiple supervision signals to ensure comprehensive motion learning across both geometric paradigms and motion scales:

$$\mathcal{L}_{\text{total}} = \mathcal{L}_{3\text{-DoF}} + \lambda_1 \mathcal{L}_{5\text{-DoF}} + \lambda_2 \mathcal{L}_{\text{flow}}. \quad (13)$$

The 3-DoF BEV-pose-loss enforces accurate planar motion estimation for ground vehicle applications through L1 regression:

$$\mathcal{L}_{3\text{-DoF}} = |t_{\text{pred},x} - t_{\text{gt},x}| + |t_{\text{pred},y} - t_{\text{gt},y}| + \alpha |\theta_{\text{pred}} - \theta_{\text{gt}}|, \quad (14)$$

where $\alpha = 10$ balances translation and rotation error magnitudes to account for the different units and typical error scales in ground vehicle motion.

The 5-DoF PV-pose-loss provides additional supervisory signals for the PV branch before LSS transformation, employing the same L1 formulation with scale normalization. To maintain consistency with monocular constraints where absolute scale information is unavailable, we supervise only the translation direction while preserving full rotational information:

$$\mathcal{L}_{5\text{-DoF}} = \|\hat{\mathbf{t}}_{\text{pred}} - \hat{\mathbf{t}}_{\text{gt}}\|_1 + \beta \|\mathbf{R}_{\text{pred}} - \mathbf{R}_{\text{gt}}\|_F, \quad (15)$$

where $\hat{\mathbf{t}} = \mathbf{t}/\|\mathbf{t}\|_2$ represents the unit-normalized translation vector, $\|\cdot\|_F$ denotes the Frobenius norm, and $\beta = 10$. This normalization strategy ensures that scale information is exclusively handled by the depth distribution estimation and BEV projection process, enabling the PV-derived correlation cost volumes and BEV correlation cost volumes to maintain compatible feature representations for effective channel-wise concatenation and fusion.

The dense flow supervision loss enforces pixel-level correspondence learning through direct L1 regression on the constructed ground truth flow field:

$$\mathcal{L}_{\text{flow}} = \|\mathbf{F}_{\text{flow}} - \mathbf{F}_{\text{flow-gt}}\|_1, \quad (16)$$

where \mathbf{F}_{flow} and $\mathbf{F}_{\text{flow-gt}}$ represent the predicted and ground truth BEV optical flow fields, respectively. The direct L1 loss formulation exploits the metric consistency of BEV representation, enabling precise pixel-level supervision without requiring additional regularization terms that could interfere with the learning of fine-grained motion patterns essential for accurate correlation-based pose estimation.

IV. EXPERIMENTS

To comprehensively validate the performance of our method across diverse testing scenarios and on carrier vehicles with different motion patterns, we select three widely-used public datasets (NCLT [16], Oxford [17], and KITTI [18]) for comparison with other MVO methods. Additionally, we collect our own multi-floor ZJH-VO Multi-Scale dataset to test the consistency and generalization of our model across different scene scales.

A. Datasets

1) Public Datasets

NCLT Dataset: The NCLT [16] dataset presents challenging conditions including significant vehicle jitter, dramatic illumination changes, and indoor-outdoor transitions. The dataset features diverse weather conditions and seasonal variations, making it suitable for generalization assessment. We train on three sequences and test on four sequences with varying degrees of weather, illumination, and path overlap with the training set. Notably, the sequence 08-20 features distinct seasonal conditions with foliage, testing our method's ability to generalize.

Oxford Dataset: The Oxford Radar RobotCar dataset [17] provides complex urban driving scenarios with varying traffic density and dynamic background participants. It evaluates MVO performance across different motion scales (long-term stops, low speed, high speed), spatial scales (alleys, streets), and conditions with numerous moving objects (following and

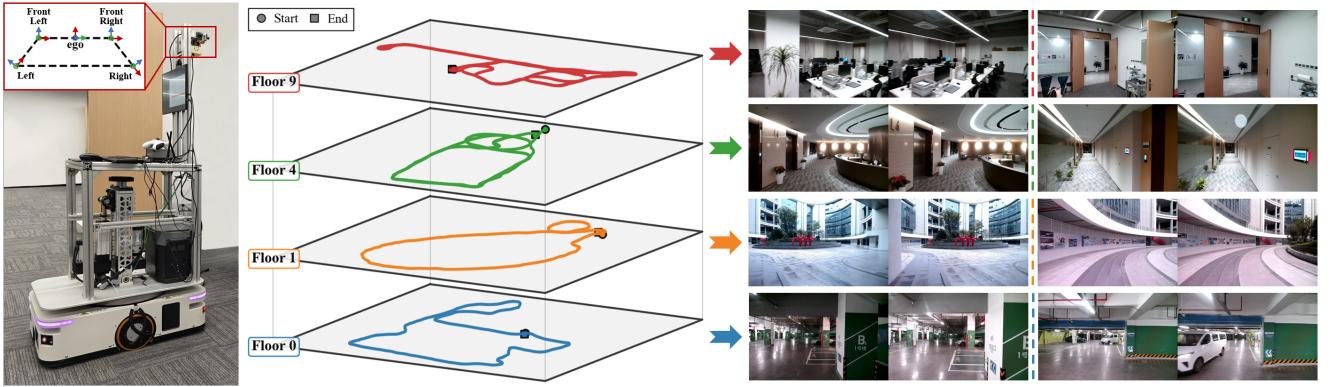


Fig. 4: ZJH-VO Multi-Scale Dataset Overview. Left: Data collection vehicle and camera coordinate system setup with PV-BEV transformation. Center: Representative trajectory paths across four floors (Floor 9, 4, 1, and 0). Right: Sample image pairs from each environment showing diverse scene characteristics.

TABLE I: ZJH-VO DATASET ENVIRONMENT CHARACTERISTICS

Environment	Object Distance	Complexity	BEV Challenge	ITS Application
Dense Office	Short range	Complex	Large rotations, texture-less walls	Last-mile Delivery
Conference Corridor	Short-Medium range	Medium	Variable lighting, narrow passages	Service Robots
Outdoor Open-Space	Long range	Medium	Sparse features, ground-dominant	Campus Navigation
Underground Garage	Medium range	Simple	Dynamic vehicles, dim lighting	Autonomous Parking

being followed). Following the same principle as NCLT, we select three training sequences and four test sequences. The sequence 17-12 includes strong illumination conditions, providing a challenging test for our method's generalization.

KITTI Dataset: The KITTI Odometry Dataset [18] serves as the standard benchmark for visual odometry evaluation, with many methods providing pretrained models and published results, enabling consistent benchmarking. Following established protocols, we train on sequences 00-08 and evaluate on sequences 09-10. These test sequences contain significant elevation changes, which challenge our 3-DoF estimation approach that assumes planar motion.

2) ZJH-VO Multi-Scale Dataset

We collect the ZJH-VO dataset using a four-wheeled mobile platform without suspension systems, equipped with a four-camera system using a hardware synchronization trigger and 2D LiDAR for ground truth generation. The camera system consists of a front-facing stereo camera pair and two additional front-left and front-right cameras with approximately 30-degree overlapping fields of view. All four cameras share identical hardware parameters and configurations, though we employ only the left camera of the front stereo pair in our experiments. The dataset encompasses 4 distinct environments across multiple floors of an office complex, including underground parking garage, outdoor plaza, conference corridors, and dense office areas. Each environment contains 3 trajectories with unique coverage areas, totaling 12 trajectories with 12,666 frames and 3,054 meters of motion data sampled at 8-frame intervals. Ground truth poses are obtained through pre-built 2D LiDAR maps and localization systems. Fig. 4 illustrates the data collection vehicle, trajectory examples from different floors, and sample frames from different floors (not adjacent frames) as examples.

Table I presents the motion characteristics of the ZJH-VO

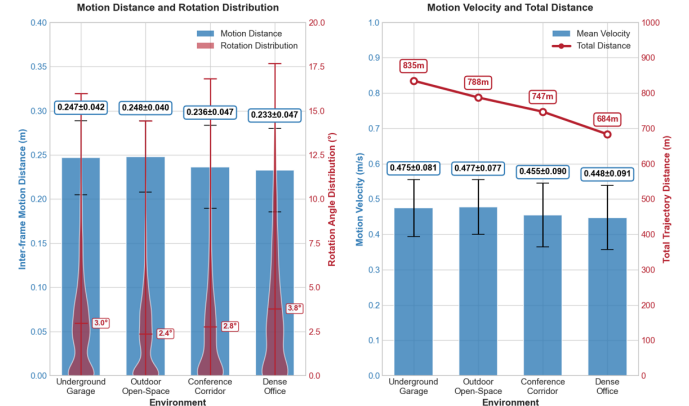


Fig. 5: ZJH-VO Multi-Scale dataset motion statistics across four environment types. Left: Inter-frame motion distance and rotation angle distributions with statistical measures. Right: Mean motion velocity and total trajectory distance for each environment sequence.

dataset across different floor scenarios. Underground Garage environments present dynamic vehicle interactions and dim lighting conditions, challenging BEV feature consistency. Outdoor Open Space scenarios test long-range feature detection with sparse distant landmarks ($\geq 10m$) and ground-dominant visual cues. Conference Corridor environments exhibit variable lighting from dark passages to bright overhead illumination, combined with floor-to-ceiling glass windows and narrow passages. Dense Office scenarios include furniture-dense layouts (0.5m-3m) with frequent large in-place rotations and corridor segments with texture-less white walls that limit feature extraction. These scenarios represent typical operational environments encountered in autonomous vehicle deployment across parking systems, campus navigation, service robotics, and last-mile delivery applications.

Fig. 5 presents motion characteristics across four environ-

ments through dual-axis visualization. The left panel shows inter-frame motion distances (bars) and rotation angle distributions (violin plots), while the right panel displays motion velocities (bars) and total trajectory distances (line plot), including inter-frame distances ranging from 0.00 to 0.31m, inter-frame rotation angles from 0.00° to 17.70°, and motion velocities from 0.00 to 0.59m/s.

We select 8 trajectories from the 12 trajectories (two from each floor) for training and utilize the remaining 4 trajectories for testing. Since the collection times and paths are not completely identical, this enables comprehensive evaluation of the same model's generalization when facing multiple scene types, as well as the adaptability of BEV-based visual representation under spatial scale variations and motion complexity commonly encountered in intelligent transportation applications.

B. Experimental Setup

1) Baselines

We compare BEV-ODOM2 with a series of mainstream traditional and learning-based MVO methods, including:

Traditional methods: ORB-SLAM3 [19], a classic feature-based SLAM system.

PV learning-based methods: Including DeepVO [22] which requires only relative pose supervision, and TartanVO [23], DF-VO [24], DROID-SLAM [25], and DPVO [26] which require additional supervision (such as depth or optical flow). These methods are all implemented under perspective view and represent the state-of-the-art in learning-based MVO.

BEV learning-based methods: BEV-DWPVO [7] and BEV-ODOM [8]. Like our current work, these methods use only pose supervision. They employ feature point extraction and matching combined with a differentiable weighted Procrustes solver, and correlation-based information extraction combined with a learning-based regression backend for pose estimation, respectively.

For a fair comparison, we disable the loop closure in ORB-SLAM3 and the global bundle adjustment in DROID-SLAM. For DF-VO, which lacks pre-trained models on the NCLT and Oxford datasets, we employ the foundation models ZoeDepth [32] and Unimatch-Flow [33] to provide depth and optical flow inputs. Specific application details for other baselines are provided in the results section for each dataset.

2) Implementation Details and Evaluation Metrics

We employ consistent hyperparameters across all public datasets, with BEV representation grid size of 128×128 and resolution of 0.8 meters, providing sufficient spatial coverage for feature mapping in BEV representation. The correlation range is set to 11×11 pixels in BEV space, capturing feature matching requirements across different motion scales. The network is built using the PyTorch framework and trained on an NVIDIA RTX 4090 GPU using the Adam optimizer with an initial learning rate of 1×10^{-4} for 100 epochs, with learning rate decay of 0.95 per epoch.

For data augmentation, we adopt the enhanced rotation sampling strategy described in Section III-F, using a 70/30 sampling ratio in favor of high-rotation pairs to ensure sufficient exposure to turning maneuvers while preventing overfitting to straight-line segments.

Evaluation metrics comprise Relative Translation Error (RTE), Relative Rotation Error (RRE), and Absolute Trajectory Error (ATE). Following standard odometry protocols, RTE and RRE are computed as the root-mean-square error (RMSE) of the relative pose over fixed-length sub-trajectories with $L \in \{100, 200, \dots, 800\}$ m. ATE is defined as the RMSE between the estimated and ground-truth trajectories after a single global alignment of the full sequence. For scale consistency assessment, we employ both SE(3) and Sim(3) alignment schemes when evaluating ATE, providing insights into whether methods can maintain accurate scale without non-causal scale corrections. Notably, for MVO methods lacking absolute scale, we scale their outputs using the first 10 meters of ground truth trajectory before any evaluation, consistent with practical deployment scenarios.

C. Qualitative Analysis and Case Study

1) Trajectory and Flow Visualization

As shown in Fig. 6, we visualize representative sequences from BEV-ODOM2 on four datasets. The predicted trajectories (red dashed lines) closely match ground truth (black solid lines), demonstrating our method's high accuracy. We further select representative segments for right turns (R), straight driving (S), and left turns (L) from each dataset's trajectory, presenting the model's predicted dense BEV optical flow fields and their error maps.

The BEV optical flow fields reveal that KITTI exhibits relatively gentle rotations, Oxford shows moderate rotations, while NCLT and ZJH-VO datasets from platforms without suspension show more dramatic rotations, consistent with expectations. These visualizations demonstrate clear motion patterns (such as arc-shaped flow fields during turns) and extremely low pixel errors (mostly below 0.4 pixels), intuitively validating the effectiveness of constructing dense supervisory signals through pose, confirming their ability to create clearer motion-representative features supporting higher-precision and more stable pose estimation. The violin plots below further illustrate inter-frame translation and rotation errors for 51-frame sequences centered on these representative segments. Thanks to Enhanced Rotation Sampling and dense supervision, errors remain consistently small across different motion patterns for each dataset.

2) Scale Consistency Analysis

Scale consistency is crucial for evaluating MVO system long-term stability. We align the scale of all PV-based methods using ground truth over the first 10 meters. As shown in Fig. 7, we plot the logarithmic scale factor variation curves for different methods on the challenging NCLT and Oxford datasets, calculated as:

$$s_i = \log_2 \left(\frac{d_i}{d_i^{\text{GT}}} \right), \quad (17)$$

where d_i and d_i^{GT} represent the estimated and ground truth displacements for segment i . The logarithmic space representation naturally accommodates the multiplicative characteristics of scale drift in MVO systems. The resulting curves illustrate how scale consistency evolves across different trajectory seg-

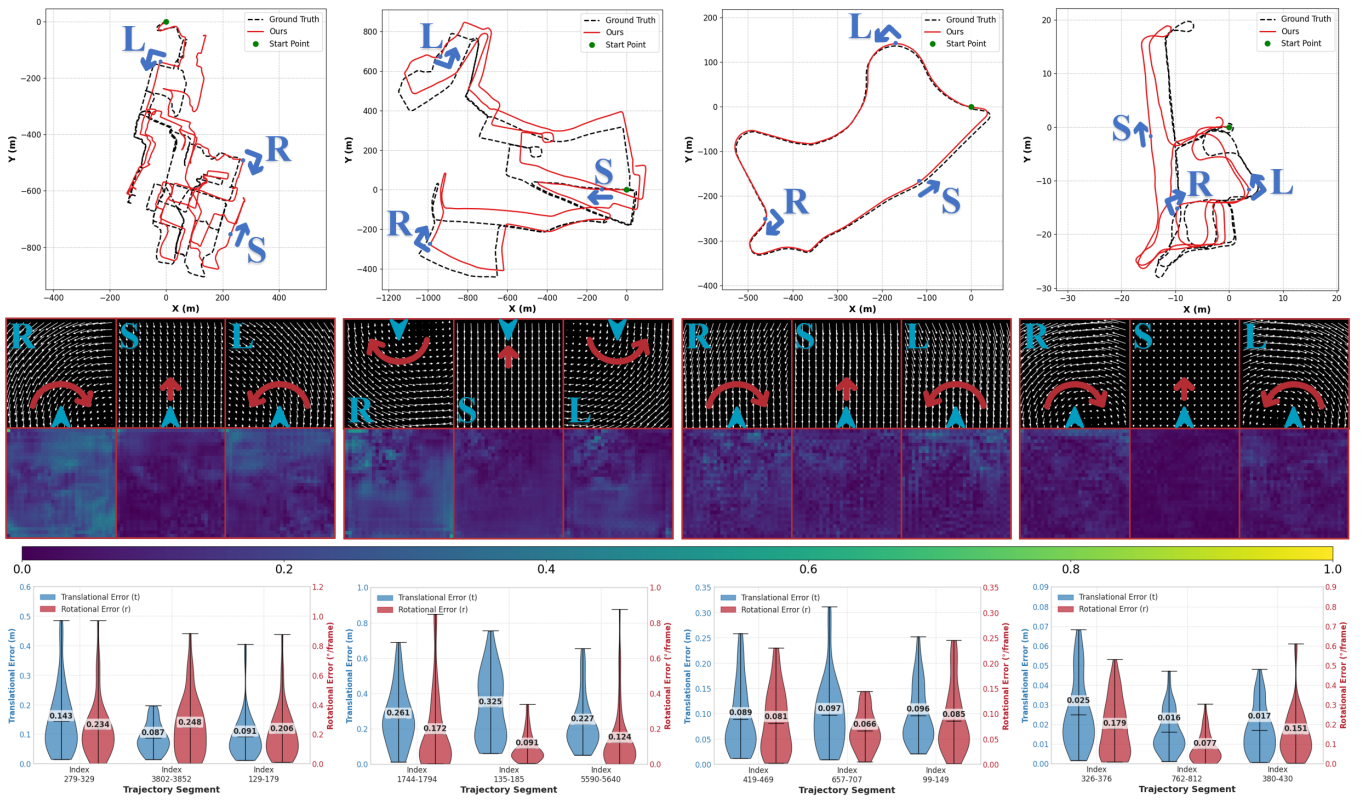


Fig. 6: Case Study of BEV-ODOM2 Performance on Four Datasets. The figure illustrates predicted trajectories for representative straight (S), left-turn (L), and right-turn (R) maneuvers. For each case, we visualize the predicted dense BEV optical flow and its corresponding error map, with most pixel errors below 0.4. Below, violin plots show the distribution of translational and rotational errors for 51-frame sequences centered on these maneuvers.

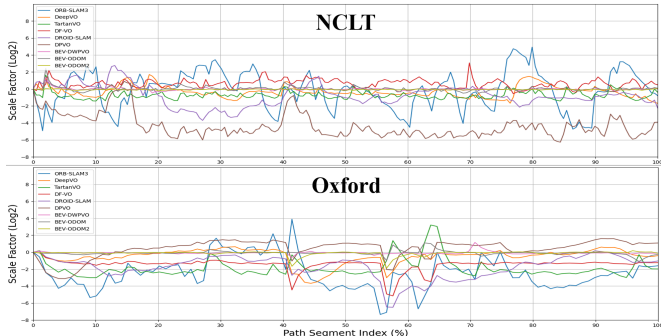


Fig. 7: Logarithmic scale factor variation on the NCLT (top) and Oxford (bottom) datasets, demonstrating the consistent low-scale-drift performance of BEV-based methods.

ments, providing insights into the long-term drift behavior of each method.

Compared to most methods, all BEV-based approaches, including BEV-DWPVO, BEV-ODOM, and BEV-ODOM2, demonstrate scale factor curves that remain closer to zero with significantly reduced fluctuations. This performance validates the effectiveness of the implicit scale anchoring strategy achieved through the BEV grid representation, which has been consistently adopted throughout our series of work. Notably, these methods achieve excellent scale consistency using only pose supervision without requiring additional supervisory signals.

Despite incorporating a more complex PV-BEV fusion architecture, BEV-ODOM2 successfully preserves this superior scale consistency characteristic. This preservation is attributed to the unified processing pipeline employed by both motion feature extraction pathways. Specifically, the BEV motion features, obtained through projection followed by correlation, and the PV motion features, derived from correlation followed by projection, both utilize the same depth estimation network and BEV representation projection mechanism. This shared pipeline ensures that all motion features are anchored to a consistent metric scale defined by the BEV grid structure, thereby maintaining scale consistency throughout the entire framework.

D. Quantitative Analysis

1) Performance on NCLT and Oxford Datasets

As shown in Table II, BEV-ODOM2 demonstrates superior performance on the challenging NCLT and Oxford datasets, achieving RTE of 5.01% and 4.60% with RRE of 2.14°/100m and 1.02°/100m, respectively.

The traditional ORB-SLAM3 method fails completely on NCLT due to feature tracking loss in high-jitter environments and suffers from severe scale drift on Oxford with numerous dynamic objects, highlighting the inherent challenges of these datasets. Among perspective view methods, those requiring auxiliary supervision signals (TartanVO, DF-VO, DROID-SLAM, DPVO) introduce additional complexity in data col-

TABLE II: PERFORMANCE COMPARISON ON NCLT AND OXFORD DATASETS

Methods	Ex. Supv.	Seq Metric	NCLT					Oxford				
			02-02	02-19	03-17	08-20	Average	11-12	15-13	16-14	17-12	Average
ORB-SLAM3 [19]	✗	RTE** (%)	/	/	/	/	/	65.22	952.41	191.75	77.44	321.70
		RRE** (°/100m)	/	/	/	/	/	19.83	10.81	16.17	19.31	16.53
DeepVO [22]	✗	RTE* (%)	31.67	18.55	21.23	25.07	24.13	25.14	27.45	31.75	37.76	30.52
		RRE* (°/100m)	14.54	8.11	9.66	13.02	11.33	7.87	8.14	11.71	12.37	10.02
TartanVO [23] (Pretrained Model)	✓	RTE** (%)	47.48	50.97	48.10	52.23	49.69	74.43	83.35	75.51	72.53	76.45
		RRE** (°/100m)	39.51	38.48	39.21	37.68	38.72	32.56	25.68	31.63	33.23	30.77
DF-VO [24] (Pre & F. Model)	✓	RTE** (%)	/	/	41.03	89.44	65.23	26.24	28.26	35.87	42.48	33.21
		RRE** (°/100m)	/	/	25.52	27.81	26.66	2.03	2.34	1.85	2.81	2.25
DROID-SLAM [25] (Pretrained Model)	✓	RTE** (%)	34.07	110.18	44.17	41.80	57.55	35.18	136.58	133.31	25.82	82.72
		RRE** (°/100m)	14.23	10.50	10.67	12.04	11.86	1.89	1.43	1.99	3.47	2.19
DPVO [26] (Pretrained Model)	✓	RTE** (%)	/	41.45	37.72	78.87	52.68	96.53	98.41	102.10	155.51	113.14
		RRE** (°/100m)	/	9.74	14.38	16.70	13.61	29.26	28.00	28.37	29.14	28.69
BEV-DWPVO [7]	✗	RTE* (%)	8.32	7.52	8.20	10.63	8.67	4.87	5.26	7.89	9.67	6.92
		RRE* (°/100m)	3.14	3.08	3.57	4.35	3.53	1.02	1.08	1.07	2.15	1.33
BEV-ODOM [8]	✗	RTE* (%)	10.89	6.27	8.77	13.89	9.95	7.21	7.90	11.55	8.02	8.67
		RRE* (°/100m)	4.74	2.47	3.73	6.31	4.31	1.38	1.89	1.14	2.55	1.74
BEV-ODOM2 (Ours)	✗	RTE* (%)	4.78	3.78	5.14	6.34	5.01	3.41	3.31	6.98	4.68	4.60
		RRE* (°/100m)	2.19	1.50	2.20	2.68	2.14	0.91	0.88	0.91	1.39	1.02

Ex. Supv.: ✓ indicates methods requiring additional supervision (depth, optical flow, segmentation), ✗ indicates pose-only supervision.

Pretrained Model: Methods utilizing pre-trained weights; **F. Model:** Foundation models for optical flow and depth estimation.

* Aligned using $SE(3)$.

** Scaled by the first 10m's ground truth and aligned using $SE(3)$.

TABLE III: PERFORMANCE COMPARISON ON KITTI ODOMETRY DATASET

Methods	Seq Metric	KITTI-09	KITTI-10	Average	KITTI-09					KITTI-10				
					RTE** (%)	RRE** (°/100m)	ATE** (m)	ATE [†] (m)	RTE** (%)	RRE** (°/100m)	ATE** (m)	ATE [†] (m)	RTE** (%)	RRE** (°/100m)
ORB-SLAM3 [19]	RTE** (%)	14.89	8.47	11.68	RTE** (%)	RRE** (°/100m)	ATE** (m)	ATE [†] (m)	RTE** (%)	RRE** (°/100m)	ATE** (m)	ATE [†] (m)	RTE** (%)	RRE** (°/100m)
	RRE** (°/100m)	1.38	0.93	1.15										
	ATE** (m)	53.69	16.15	34.92										
	ATE [†] (m)	40.63	7.33	23.98										
DeepVO [22]	RTE* (%)	33.55	30.46	32.01	RTE* (%)	RRE* (°/100m)	ATE* (m)	ATE [†] (m)	RTE* (%)	RRE* (°/100m)	ATE* (m)	ATE [†] (m)	RTE* (%)	RRE* (°/100m)
	RRE* (°/100m)	14.31	14.42	14.37										
	ATE* (m)	59.38	180.10	119.74										
	ATE [†] (m)	51.58	168.44	110.01										
TartanVO [23] (Original Paper)	RTE* (%)	6.00	6.89	6.45	RTE* (%)	RRE* (°/100m)	ATE* (m)	ATE [†] (m)	RTE* (%)	RRE* (°/100m)	ATE* (m)	ATE [†] (m)	RTE* (%)	RRE* (°/100m)
	RRE* (°/100m)	3.11	2.73	2.92										
	ATE* (m)	53.84	28.50	41.17										
	ATE [†] (m)	27.52	23.65	25.59										
DF-VO [24] (Original Paper)	RTE* (%)	2.40	1.82	2.11	RTE* (%)	RRE* (°/100m)	ATE* (m)	ATE [†] (m)	RTE* (%)	RRE* (°/100m)	ATE* (m)	ATE [†] (m)	RTE* (%)	RRE* (°/100m)
	RRE* (°/100m)	0.24	0.38	0.31										
	ATE* (m)	7.73	3.00	5.37										
	ATE [†] (m)	7.65	2.73	5.19										
DROID-SLAM [25] (Pretrained Model)	RTE** (%)	21.01	18.73	19.87	RTE** (%)	RRE** (°/100m)	ATE** (m)	ATE [†] (m)	RTE** (%)	RRE** (°/100m)	ATE** (m)	ATE [†] (m)	RTE** (%)	RRE** (°/100m)
	RRE** (°/100m)	0.33	0.23	0.28										
	ATE** (m)	73.71	45.52	59.61										
	ATE [†] (m)	74.31	17.27	45.79										
DPVO [26] (Pretrained Model)	RTE** (%)	17.70	4.47	11.09	RTE** (%)	RRE** (°/100m)	ATE** (m)	ATE [†] (m)	RTE** (%)	RRE** (°/100m)	ATE** (m)	ATE [†] (m)	RTE** (%)	RRE** (°/100m)
	RRE** (°/100m)	0.24	0.23	0.23										
	ATE** (m)	64.80	10.98	37.89										
	ATE [†] (m)	64.77	10.99	37.88										
BEV-DWPVO [7]	RTE* (%)	2.13	3.24	2.69	RTE* (%)	RRE* (°/100m)	ATE* (m)	ATE [†] (m)	RTE* (%)	RRE* (°/100m)	ATE* (m)	ATE [†] (m)	RTE* (%)	RRE* (°/100m)
	RRE* (°/100m)	0.65	1.15	0.90										
	ATE* (m)	8.69	9.04	8.87										
	ATE [†] (m)	8.11	7.80	7.96										
BEV-ODOM [8]	RTE* (%)	1.72	3.61	2.67	RTE* (%)	RRE* (°/100m)	ATE* (m)	ATE [†] (m)	RTE* (%)	RRE* (°/100m)	ATE* (m)	ATE [†] (m)	RTE* (%)	RRE* (°/100m)
	RRE* (°/100m)	0.39	0.53	0.46										
	ATE* (m)	6.35	8.42	7.39										
	ATE [†] (m)	4.62	7.30	5.96										
BEV-ODOM2 (Ours)	RTE* (%)	1.37	3.46	2.42	RTE* (%)	RRE* (°/100m)	ATE* (m)	ATE [†] (m)	RTE* (%)	RRE* (°/100m)	ATE* (m)	ATE [†] (m)	RTE* (%)	RRE* (°/100m)
	RRE* (°/100m)	0.35	0.52	0.44										
	ATE* (m)	2.89	6.08	4.49										
	ATE [†] (m)	2.72	5.97	4.35										

Original Paper: Results as reported in the original publication;

Pretrained Model: Results obtained using pretrained weights.

* Aligned using $SE(3)$.

** Scaled by the first 10m's ground truth and aligned using $SE(3)$.

† Aligned using $Sim(3)$.

lection and system deployment, while DeepVO, which uses pose-only supervision like our method, demonstrates inferior performance compared to BEV-based approaches. Within BEV methods, our approach provides denser supervision compared to BEV-ODOM and offers more flexible constraints compared to BEV-DWPVO's solver while incorporating PV branch information through correlation-based fusion. This leads to notable improvements with RTE reductions of 42.21% and 33.53% over existing BEV-based methods that rely solely on 3-DoF motion modeling and pose supervision, and RRE reductions of 39.38% and 23.31%, respectively.

2) Performance on KITTI Dataset

As presented in Table III, BEV-ODOM2 also performs exceptionally well on the KITTI dataset. On the loop sequence 09, it achieves the best results for both RTE and ATE metrics. Although its precision on sequence 10, which features significant elevation changes, is lower than that of DF-VO (trained with stereo data and depth/flow supervision), this is consistent with the expectations for our 3-DoF motion model. Nevertheless, our method demonstrates exceptional scale consistency with an average ATE of 4.49m under $SE(3)$ alignment. Remarkably, this performance, achieved without any ground truth scale information, surpasses most baseline methods that employ $Sim(3)$ alignment with ground truth scale correction. The performance gain over BEV-ODOM confirms that the introduction of PV information helps the network integrate information about non-planar motion.

3) Performance on ZJH-VO Dataset

For experiments on the ZJH-VO dataset, to reduce the generalization impact of pretrained models from learning-based methods in new scenes, we compare multiple optical flow foundation models and select the best-performing Unimatch-Flow to generate optical flow ground truth. We fine-tune TartanVO based on its pretrained model, achieving significant improvement over pose-only supervised DeepVO,

TABLE IV: ABLATION STUDY ON THREE DATASETS

Enhanced Rotation Sampling	Dense Flow Supervision	PV-BEV Fusion	NCLT			Oxford			ZJH-VO		
			RTE* (%)	RRE* (/100m)	ATE [†] (m)	RTE* (%)	RRE* (/100m)	ATE [†] (m)	RTE* (%)	RRE* (/100m)	ATE [†] (m)
✗	✗	✗	9.95	4.31	126.63	8.67	1.74	108.35	7.28	7.98	3.68
✓	✗	✗	6.68	3.08	105.00	6.51	1.17	101.80	5.85	6.29	2.86
✓	✓	✗	5.09	2.17	72.95	5.08	1.09	86.51	4.13	5.19	2.29
✓	✓	✓	5.01	2.14	63.95	4.60	1.02	70.57	3.57	4.69	2.04

Enhanced Rotation Sampling: Rotation-aware sampling strategy to balance diverse motion patterns and address dataset bias.

Dense Flow Supervision: Pixel-level BEV optical flow supervision constructed from pose ground truth for dense correspondence learning.

PV-BEV Fusion: Dual-branch fusion that preserves 6-DoF motion information while maintaining BEV representation advantages.

* Aligned using $SE(3)$; [†] Aligned using $Sim(3)$.

TABLE V: PERFORMANCE COMPARISON ON ZJH-VO MULTI-SCALE ODOMETRY DATASET

Methods	Seq Metric	F-09	F-04	F-01	F-00	Average
ORB-SLAM3 [19] (Partial)	RTE** (%)	9.63	14.76	4.57	6.77	8.94
	RRE** (/100m)	13.67	28.26	6.95	7.97	14.21
	ATE** (m)	6.34	5.73	2.03	3.00	4.28
	ATE [†] (m)	6.12	5.54	1.91	1.66	3.81
DeepVO [22] (Retrained)	RTE* (%)	51.05	37.52	56.08	63.16	51.95
	RRE* (/100m)	106.52	116.07	102.27	111.58	109.11
	ATE* (m)	25.65	18.71	14.72	21.17	20.06
	ATE [†] (m)	10.79	10.04	14.36	15.81	12.75
TartanVO [23] (Retrained)	RTE* (%)	5.98	5.27	23.27	6.71	10.31
	RRE* (/100m)	14.76	18.46	29.79	6.58	17.40
	ATE* (m)	3.52	3.16	14.00	2.48	5.79
	ATE [†] (m)	3.48	3.14	11.70	2.19	5.13
DF-VO [24] (F. Model)	RTE** (%)	31.31	105.42	55.16	48.11	60.00
	RRE** (/100m)	88.26	141.32	117.93	75.13	105.66
	ATE** (m)	116.79	64.45	45.99	19.71	36.73
	ATE [†] (m)	10.56	11.96	24.02	18.94	16.37
DROID-SLAM [25] (Pretrained Model)	RTE** (%)	16.85	6.98	14.15	25.00	15.75
	RRE** (/100m)	25.50	26.36	6.15	30.44	22.11
	ATE** (m)	12.52	8.91	8.82	17.00	11.81
	ATE [†] (m)	11.65	8.33	<u>3.57</u>	10.78	8.58
DPVO [26] (Pretrained Model)	RTE** (%)	14.67	6.55	11.08	26.65	14.74
	RRE** (/100m)	53.48	<u>3.33</u>	<u>4.37</u>	17.42	19.65
	ATE** (m)	11.11	7.46	<u>6.94</u>	18.08	10.90
	ATE [†] (m)	11.10	6.08	<u>3.20</u>	12.29	8.16
BEV-ODOM [8]	RTE* (%)	<u>1.91</u>	3.47	20.29	<u>3.46</u>	7.28
	RRE* (/100m)	6.39	<u>7.83</u>	13.28	<u>4.41</u>	7.98
	ATE* (m)	<u>1.15</u>	<u>2.00</u>	11.00	<u>1.63</u>	<u>3.95</u>
	ATE [†] (m)	<u>1.12</u>	<u>1.91</u>	10.94	<u>0.77</u>	<u>3.68</u>
Ours	RTE* (%)	2.07	<u>2.73</u>	8.23	<u>1.24</u>	3.57
	RRE* (/100m)	<u>5.48</u>	7.94	<u>4.05</u>	<u>1.28</u>	4.69
	ATE* (m)	<u>1.35</u>	<u>1.55</u>	<u>4.89</u>	<u>0.67</u>	<u>2.11</u>
	ATE [†] (m)	<u>1.35</u>	<u>1.55</u>	4.67	<u>0.57</u>	<u>2.04</u>

Partial: Method did not complete full sequence evaluation;

Retrained: Methods retrained on this dataset to obtain new models;

Pretrained Model: Methods utilizing pre-trained weights;

F. Model: Foundation models for optical flow and depth estimation.

* Aligned using $SE(3)$.

** Scaled by the first 10m's ground truth and aligned using $SE(3)$.

† Aligned using $Sim(3)$.

but still show a gap compared to our proposed method. ORB-SLAM3 experiences feature tracking loss in all scenarios, so we only show metrics for successful portions after cropping and alignment.

As shown in Table V, the advantages of BEV-ODOM2 are further validated on the ZJH-VO multi-scale dataset, built for real-world intelligent transportation applications. It achieves the best performance on the average metrics, which represent generalization capability across multiple scenes. Compared to BEV-ODOM using only sparse pose supervision, dense BEV optical flow supervision provides richer supervisory signals, enabling the network to learn clearer mappings of objects at different distances in BEV representation during training. This enhanced feature representation not only improves pose estimation accuracy but also maintains exceptional scale consistency. Despite the challenging multi-scale environment that

tests BEV grid representation limits, BEV-ODOM2 achieves superior ATE under $SE(3)$ alignment compared to most methods using ground truth scale correction, confirming the robustness of our approach across diverse operational conditions.

E. Ablation Study

To verify the effectiveness of each core component in BEV-ODOM2, we conduct ablation experiments on public datasets NCLT, Oxford and our collected ZJH-VO dataset, with results shown in Table IV. The baseline model (first row) is an implementation without any new features.

Effect of Enhanced Rotation Sampling: Introducing the enhanced rotation sampling strategy (second row) improves RTE, RRE, and ATE metrics across all datasets. This confirms that balancing the motion patterns in the training data effectively mitigates dataset bias and enhances the model's ability to estimate less frequent but critical actions like turns.

Effect of Dense Flow Supervision: After adding dense BEV optical flow supervision (third row), performance shows further significant improvement. All datasets demonstrate over 20% improvement in RTE metrics, especially for the multi-scale, multi-scene ZJH-VO dataset, where RTE improvement reaches nearly 30%. This demonstrates that our proposed constructible dense supervision signals provide dense, pixel-level correspondence information for the network, greatly enhancing its learning capability for fine motion patterns, especially bringing more precise BEV mapping and representation capabilities for dataset scenarios with extensive feature distance spans. The introduction of BEV optical flow supervision also brings stability improvements, corresponding to significant ATE improvements across four trajectories on each dataset, intuitively indicating that predicted trajectories are overall closer to ground truth, showing more stable performance in pose estimation across the entire pipeline.

Effect of PV-BEV Fusion: Finally, after fusing PV branch information (fourth row, complete BEV-ODOM2), model performance reaches optimal levels. This indicates that the PV branch successfully compensates for information loss in non-primary degrees of freedom such as pitch and roll in BEV representation by extracting correlation information before projection to the BEV plane. By fusing features from both branches, the model can more comprehensively understand the vehicle's complete motion state, enabling more accurate 3-DoF pose estimation. Although the improvement is more modest compared to sampling and supervision strategies, consistent gains across all metrics prove the value of preserving rich motion information lost during LSS transformation. This com-

ponent is particularly beneficial for complex motion pattern scenarios requiring comprehensive geometric understanding.

V. CONCLUSION AND FUTURE WORK

This paper introduces BEV-ODOM2, a monocular visual odometry framework that significantly improves upon existing BEV-based methods. Our approach incorporates two key innovations: (1) dense BEV optical flow supervision constructed directly from pose ground truth, which provides dense, pixel-level guidance without extra annotations; and (2) a PV-BEV fusion strategy that preserves 6-DoF motion cues to mitigate information loss during BEV projection. Extensive evaluations show that BEV-ODOM2 achieves a 40% improvement in relative translation error over prior BEV methods while maintaining the robust scale consistency inherent to the BEV representation. An enhanced rotation sampling strategy further ensures robust performance across diverse motion patterns.

To facilitate future research, we release the ZJH-VO dataset, a comprehensive multi-scene, multi-scale benchmark for ground vehicle visual odometry. Alongside the dataset, we open-source the associated calibration results and provide performance baselines from representative MVO methods.

Future work will focus on enhancing long-term robustness by integrating multi-camera systems for 360-degree perception, incorporating relocalization and loop closure capabilities to correct accumulated drift, and developing adaptive temporal models for stability in adverse conditions. These steps aim to transition BEV-ODOM2 from a research prototype to a production-ready system for reliable navigation in intelligent transportation applications.

REFERENCES

- [1] J. Ross, O. Mendez, A. Saha, M. Johnson, and R. Bowden, “Bev-slam: Building a globally-consistent world map using monocular vision,” in *2022 IEEE/RSJ International Conference on Intelligent Robots and Systems (IROS)*. IEEE, 2022, pp. 3830–3836.
- [2] N. Chen, J. Wang, H. Chen, Y. Shen, S. Wang, and X. Tan, “Bevloc: End-to-end 6-dof localization via cross-modality correlation under bird’s eye view,” in *IEEE International Conference on Acoustics, Speech and Signal Processing (ICASSP)*, 2024.
- [3] Z. Zhang, M. Xu, W. Zhou, T. Peng, L. Li, and S. Poslad, “Bev-locator: An end-to-end visual semantic localization network using multi-view images,” *Science China Information Sciences*, vol. 68, no. 2, p. 122106, 2025.
- [4] D. Scaramuzza and F. Fraundorfer, “Visual odometry [tutorial],” *IEEE robotics & automation magazine*, vol. 18, no. 4, pp. 80–92, 2011.
- [5] C. Chen, B. Wang, C. X. Lu, N. Trigoni, and A. Markham, “A survey on deep learning for localization and mapping: Towards the age of spatial machine intelligence,” *arXiv preprint arXiv:2006.12567*, 2020.
- [6] D. Unger, N. Gosalha, V. R. Kumar, S. Borse, A. Valada, and S. Yogamani, “Multi-camera bird’s eye view perception for autonomous driving,” *Computer Vision: Challenges, Trends, and Opportunities*, p. 279, 2024.
- [7] Y. Wei, S. Lu, W. Lu, R. Xiong, and Y. Wang, “Bev-dwpvo: Bev-based differentiable weighted procrustes for low scale-drift monocular visual odometry on ground,” *IEEE Robotics and Automation Letters*, 2025.
- [8] Y. Wei, S. Lu, F. Han, R. Xiong, and Y. Wang, “Bev-odom: Reducing scale drift in monocular visual odometry with bev representation,” in *2024 IEEE/RSJ International Conference on Intelligent Robots and Systems (IROS)*. IEEE, 2024, pp. 349–356.
- [9] K. Tateno, F. Tombolini, I. Laina, and N. Navab, “Cnn-slam: Real-time dense monocular slam with learned depth prediction,” in *Proceedings of the IEEE conference on computer vision and pattern recognition*, 2017, pp. 6243–6252.
- [10] B. Bescos, J. M. Fácil, J. Civera, and J. Neira, “Dynaslam: Tracking, mapping, and inpainting in dynamic scenes,” *IEEE Robotics and Automation Letters*, vol. 3, no. 4, pp. 4076–4083, 2018.
- [11] S. Wang, V. Leroy, Y. Cabon, B. Chidlovskii, and J. Revaud, “Dust3r: Geometric 3d vision made easy,” in *Proceedings of the IEEE/CVF Conference on Computer Vision and Pattern Recognition*, 2024, pp. 20697–20709.
- [12] J. Philion and S. Fidler, “Lift, splat, shoot: Encoding images from arbitrary camera rigs by implicitly unprojecting to 3d,” in *Computer Vision–ECCV 2020: 16th European Conference, Glasgow, UK, August 23–28, 2020, Proceedings, Part XIV 16*. Springer, 2020, pp. 194–210.
- [13] Y. Li, Z. Ge, G. Yu, J. Yang, Z. Wang, Y. Shi, J. Sun, and Z. Li, “Bevdepth: Acquisition of reliable depth for multi-view 3d object detection,” in *Proceedings of the AAAI Conference on Artificial Intelligence*, vol. 37, no. 2, 2023, pp. 1477–1485.
- [14] D. Sun, X. Yang, M.-Y. Liu, and J. Kautz, “Pwc-net: Cnn for optical flow using pyramid, warping, and cost volume,” in *Proceedings of the IEEE conference on computer vision and pattern recognition*, 2018, pp. 8934–8943.
- [15] Z. Teed and J. Deng, “Raft: Recurrent all-pairs field transforms for optical flow,” in *European conference on computer vision*. Springer, 2020, pp. 402–419.
- [16] N. Carlevaris-Bianco, A. K. Ushani, and R. M. Eustice, “University of michigan north campus long-term vision and lidar dataset,” *The International Journal of Robotics Research*, vol. 35, no. 9, pp. 1023–1035, 2016.
- [17] W. Maddern, G. Pascoe, C. Linegar, and P. Newman, “1 year, 1000 km: The oxford robotcar dataset,” *The International Journal of Robotics Research*, vol. 36, no. 1, pp. 3–15, 2017.
- [18] A. Geiger, P. Lenz, C. Stiller, and R. Urtasun, “Vision meets robotics: The kitti dataset,” *The International Journal of Robotics Research*, vol. 32, no. 11, pp. 1231–1237, 2013.
- [19] C. Campos, R. Elvira, J. J. G. Rodríguez, J. M. Montiel, and J. D. Tardós, “Orb-slam3: An accurate open-source library for visual, visual–inertial, and multimap slam,” *IEEE Transactions on Robotics*, vol. 37, no. 6, pp. 1874–1890, 2021.
- [20] J. Engel, V. Koltun, and D. Cremers, “Direct sparse odometry,” *IEEE transactions on pattern analysis and machine intelligence*, vol. 40, no. 3, pp. 611–625, 2017.
- [21] C. Forster, M. Pizzoli, and D. Scaramuzza, “Svo: Fast semi-direct monocular visual odometry,” in *2014 IEEE international conference on robotics and automation (ICRA)*. IEEE, 2014, pp. 15–22.
- [22] S. Wang, R. Clark, H. Wen, and N. Trigoni, “Deepvo: Towards end-to-end visual odometry with deep recurrent convolutional neural networks,” in *2017 IEEE international conference on robotics and automation (ICRA)*. IEEE, 2017, pp. 2043–2050.
- [23] W. Wang, Y. Hu, and S. Scherer, “Tartanvo: A generalizable learning-based vo,” in *Conference on Robot Learning*. PMLR, 2021, pp. 1761–1772.
- [24] H. Zhan, C. S. Weerasekera, J.-W. Bian, R. Garg, and I. Reid, “Df-vo: What should be learnt for visual odometry?” *arXiv preprint arXiv:2103.00933*, 2021.
- [25] Z. Teed and J. Deng, “Droid-slam: Deep visual slam for monocular, stereo, and rgb-d cameras,” *Advances in neural information processing systems*, vol. 34, pp. 16558–16569, 2021.
- [26] Z. Teed, L. Lipson, and J. Deng, “Deep patch visual odometry,” *Advances in Neural Information Processing Systems*, vol. 36, 2024.
- [27] H. Li, Y. Duan, X. Zhang, H. Liu, J. Ji, and Y. Zhang, “Occ-vo: Dense mapping via 3d occupancy-based visual odometry for autonomous driving,” *arXiv preprint arXiv:2309.11011*, 2023.
- [28] J. C. Gower, “Generalized procrustes analysis,” *Psychometrika*, vol. 40, pp. 33–51, 1975.
- [29] K. He, X. Zhang, S. Ren, and J. Sun, “Deep residual learning for image recognition,” in *Proceedings of the IEEE conference on computer vision and pattern recognition*, 2016, pp. 770–778.
- [30] T.-Y. Lin, P. Dollár, R. Girshick, K. He, B. Hariharan, and S. Belongie, “Feature pyramid networks for object detection,” in *Proceedings of the IEEE conference on computer vision and pattern recognition*, 2017, pp. 2117–2125.
- [31] O. Ronneberger, P. Fischer, and T. Brox, “U-net: Convolutional networks for biomedical image segmentation,” in *Medical image computing and computer-assisted intervention–MICCAI 2015: 18th international conference, Munich, Germany, October 5–9, 2015, proceedings, part III 18*. Springer, 2015, pp. 234–241.
- [32] S. F. Bhat, R. Birk, D. Wofk, P. Wonka, and M. Müller, “Zoedepth: Zero-shot depth by combining relative and metric depth,” *arXiv preprint arXiv:2302.12288*, 2023.
- [33] H. Xu, J. Zhang, J. Cai, H. Rezatofighi, F. Yu, D. Tao, and A. Geiger, “Unifying flow, stereo and depth estimation,” *IEEE Transactions on Pattern Analysis and Machine Intelligence*, 2023.